Supporting information

Low Pt loading with lattice strain for direct ethylene glycol fuel cell

Hao Lei[a‡], Ninggui Ma[b‡], Kaikai Li[a], Yu Wang[a], Qunhui Yuan[a], Jun Fan[b*], Jianglan Shui[c], Yan Huang[a,d,e*]

Affiliations

[a] Sauvage Laboratory for Smart Materials, School of Materials Science and Engineering, Harbin Institute of Technology (Shenzhen), Shenzhen 518055, China.

[b] Department of Materials Science and Engineering, City University of Hong Kong, Hong Kong 999077, China.

[c] School of Materials Science and Engineering, Beihang University, Beijing 100191, China.

[d] State Key Laboratory of Advanced Welding and Joining, Harbin Institute of Technology (Shenzhen), Shenzhen 518055, China.

[e] Shenzhen Key Laboratory of Flexible Printed Electronics Technology, Harbin Institute of Technology (Shenzhen), Shenzhen 518055, China.

‡ These authors contributed equally to this work.

* Corresponding author. E-mail: junfan@cityu.edu.hk; yanhuanglib@hit.edu.cn

Experimental Section

Synthesis of Pt-Fe

Pt-Fe was prepared by a simple two-step process. The first step is the deposition of 0.4 C cm^{-2} charged metallic Fe on a Ni plate by constant voltage electrochemical deposition (-0.8 V vs. Ag^{+}) using an electrochemical workstation. The process was carried out in an ethaline solution (typical deep eutectic solvent ethaline was obtained by stirring ethylene glycol (EG) and choline chloride in a 2:1 molar ratio for 2 h at 353 K) containing 0.1 M $FeCl_3$ using a three-electrode system (working electrode: Ni plate, counter electrode: carbon rod, reference electrode: Ag wire (Φ=1 mm)).

In the second step, the prepared Fe/Ni was placed in EG solution containing 0.1 mM $H_2PtCl_6 \cdot 6H_2O$ for 10 h. The prepared catalyst was washed repeatedly in water and ethanol to obtain the Pt-Fe catalyst. Pt was loaded on the Fe/Ni substrate by a displacement reaction. The metal Fe is located prior to Pt in the metal activity sequence, meaning that Fe has the ability to displace Pt ions. During the replacement of Pt ions in solution by metallic Fe, Fe atoms lost electrons to form positively valenced Fe ions. Pt ions in the solution accepted electrons from Fe, which reduces them to the Pt metal.

In order to optimize the Pt-Fe preparation parameters, we followed the performance-oriented principle and carried out experiments on the key parameters affecting Pt and Fe loadings (i.e., the charge density of deposited Fe, the voltage of deposited Fe, and the immersion time of Pt replacement deposition) (Fig. S1).

Synthesis of ET-Pt-Fe

ET-Pt-Fe was obtained by placing Pt-Fe in 1 M KOH+1 M EG solution for 50 cyclic voltammetry scans (scanning range of 0.15-1.3 V vs. RHE, scanning rate of 50 mV s^{-1}). The optimal number of electrochemical tuning and the compositional changes of ET-Pt-Fe during the tuning process were also explored (Fig. S2). The optimum number of electrochemical tunings was determined to be 50 cycles (Fig. S3).

Characterization

The structure and morphology of samples were measured using a scanning electron microscope (SEM, QUANTA Q400) and a transmission electron microscope (TEM, FEI Tecnai G2 F20). The phase composition and electronic structure of samples were investigated by X-ray photoelectron spectroscopy (XPS, EscaLab 250Xi) under the excitation of Al Kα X-ray radiation (hv =1486.6 eV). The inductively coupled plasma mass spectrometry (ICP MS, PerkinElmer ELAN DRC-e,) was used to detect the content of each element in the samples. Fe vacancies in the samples were determined using an electron spin paramagnetic resonance spectrometer (EPR, JES-FA200). Electrochemical *in situ* Fourier transform infrared (FT-IR) reflectance spectroscopy measurements were recorded using a Nexus 870 spectrometer (Nicolet) equipped with a liquid nitrogen cooled MCT-A detector. Individual IR spectra were obtained with a resolution of 4 cm^{-1} by superimposing 64 scans, and due to the strong absorption of the IR light by the electrolyte, the test procedure required an appropriate gain adjustment to obtain a moderate IR intensity. A three-electrode *in-situ* cell was used for the electrochemical reaction and cyclic voltammetry was performed on the *in-situ* cell

using an electrochemical workstation (model: CHI 760E) to provide an electrochemical signal. *In-situ* IR spectra were taken at a frequency of 200 s, i.e. one IR pattern per every 0.1 V. After each cycle, the sample was left to settle until the voltage stabilized and the background was taken again before continuing with the IR test.

Electrochemical measurements

The electrocatalytic oxidation of alcohols (EG and methanol) was carried out on a CHI 660E electrochemical workstation at room temperature and ambient pressure in a three-electrode system: the synthetic catalyst was the working electrode, the carbon rod electrode (1 × 1 cm^2) was the counter electrode, the Ag/AgCl electrode (3 M KCI solution) was the reference electrode and the electrolyte was a mixture of 1 M KOH and 1 M EG or methanol. All measured potentials were converted to the RHE using $E_{vs.\ RHE} = E_{vs.\ Ag/AgCl} + 0.198 + 0.059 \times pH$[1]. The CO stripping voltammetry was collected in the 1 M KOH solution. High-purity CO (99.99 %) was bubbled into the electrolyte over 20 min. Then, the excess CO in KOH solution was purged out using N_2 over 10 min. The CO stripping was obtained in 0 ~ 1.3 V vs. RHE.

Commercial Pt/C electrode was prepared by two steps. In the first step, Pt/C (4 mg) and Nafion (30 uL, 5 wt.%) were dispersed in 0.47 mL isopropyl alcohol solution and ultrasonic treatment was conducted for 10 min to obtain homogeneous catalyst ink. The nickel plate (working area: 0.5 cm^2) was then loaded with an appropriate amount of catalyst ink to give a platinum mass loading of 26 μg cm^{-2}.

Membrane electrode assembly and direct ethylene glycol fuel cell tests

Prior to fuel cell performance testing, the anode catalyst was prepared by mixing 1 mg of ET-Pt-Fe (ET-Pt-Fe was stripped from the nickel plate by ultrasonic technology and subsequently collected by filtration), 5 mg of Vulcan XC-72 carbon, and 40 μL of Nafion solution (5 wt.%) in 600 μL of isopropanol and sonicated for 1 h. Subsequently, the 67 μL slurry was then evenly dropped onto each piece of nickel foam (1 cm × 1 cm, thickness: 0.5 mm, pore size: 200 μm; porosity: 98%). The loading of Pt on the ET-Pt-Fe electrode was 0.1 mg cm^{-2}. For comparison, 5 mg of industrial grade Pt/C (20 wt.%) and 40 μL of Nafion solution (5 wt.%) were dispersed into 600 μL of isopropanol. After sonication for 1 h, 640 μL of the slurry was dropped onto the nickel foam. The loading of Pt on the Pt/C electrode was 1 mg cm^{-2}. Similarly, 2 mg of S-C_3N_4/CNT and 16 μL of Nafion solution (5 wt.%) were dispersed in 600 μl of isopropanol solution and then added dropwise onto a gas diffusion layer (1 cm × 1 cm) to obtain the cathode catalyst. The loading of S-C_3N_4/CNT electrode was 2 mg cm^{-2}. The commercial Fumasep FAAM-15 membrane was used as the anion exchange membrane in the membrane electrode assembly (MEA). Finally, the MEA was made by sandwiching the Fumasep FAAM-15 membrane between the ET-Pt-Fe anode and the S-C_3N_4/CNT cathode and hot pressing it at 80 °C and 1 MPa for 40 s.

Performance and stability of the DEGFC were determined by a fuel cell test system (850e, Scribner Associates Inc.). 3 M EG mixed with 6 M KOH (0.5 mL min^{-1}) was pumped to the anode while oxygen (50 mL min^{-1}) was supplied to the cathode, which was fully humidified and the cell temperature was maintained at 80 °C. During the

continuous operation of the fuel cell, the anolyte was refreshed every 10 hours to avoid the potential influence of carbonate and ensure stable performance.

DFT calculations

The calculations in this study were conducted using the *ab initio* simulation package (VASP) [2], based on density functional theory (DFT). Specifically, the projector augmented wave (PAW) method was employed to account for the interaction of nuclear and valence electrons[3], and the exchange–correlation functional was described using the generalized gradient approximation (GGA) with Perdew–Burke–Ernzerhof (PBE) parametrization[4]. A cutoff energy of 450 eV was applied to the expanded plane-wave basis. During structural optimization, the energy and force convergence criteria were set to less than 10^{-5} eV and 0.02 eV/Å, respectively. The (112) surface of Fe_2O_3, as determined by XRD results (comprising 72 O atoms and 48 Fe atoms), was selected as the studied surface. Structural optimization utilized a gamma-centered denser 1×1×1 K-point[5]. In the z direction, a 20 Å vacuum layer was introduced to prevent periodic interactions. Additionally, to account for non-bonding interactions between atoms, the DFT-D3 approach was employed to model van der Waals interactions, providing correction to the dispersion relation[6]. Bader charge population analysis was adopted to describe electron transfer. The adsorption energy is calculated as follows:

$$E_{ads} = E_{*ad} - E_{slab} - E_{ad}$$

Where E_{*ad} is the total energy of the Fe_2O_3 with Pt atom, E_{slab} is the total energy of Fe_2O_3. E_{ad} is energy of Pt atom. The energy of Pt atoms is from bulk phase materials.

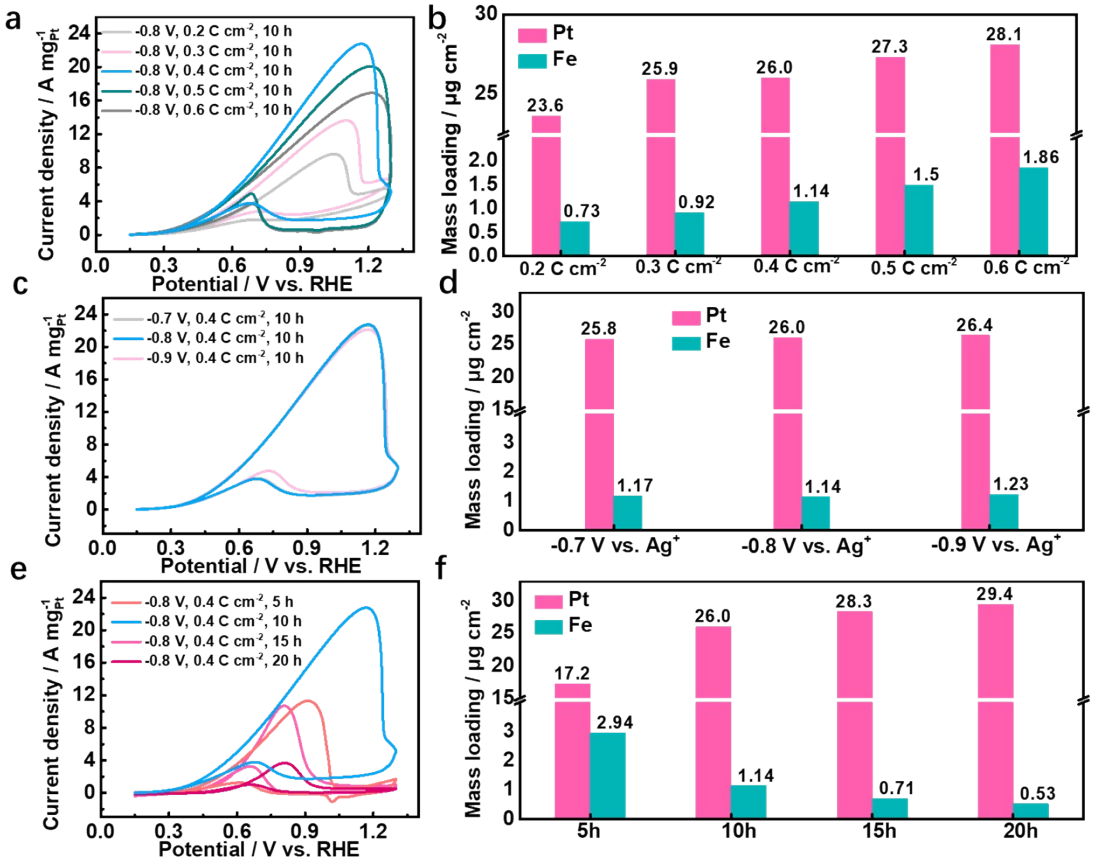

Fig. S1. Effect of (a) electrochemical deposition of Fe with different charge densities, (c) different potentials of electrochemical deposition of Fe and (e) replacement deposition of Pt with different times on the EG oxidation performance of Pt-Fe electrocatalysts. Effect of variation of preparation conditions on the loading of each element in the catalyst: (b) electrochemical deposition of Fe with different charge densities; (d) different potentials of electrochemical deposition of Fe; and (f) replacement deposition of Pt with different times.

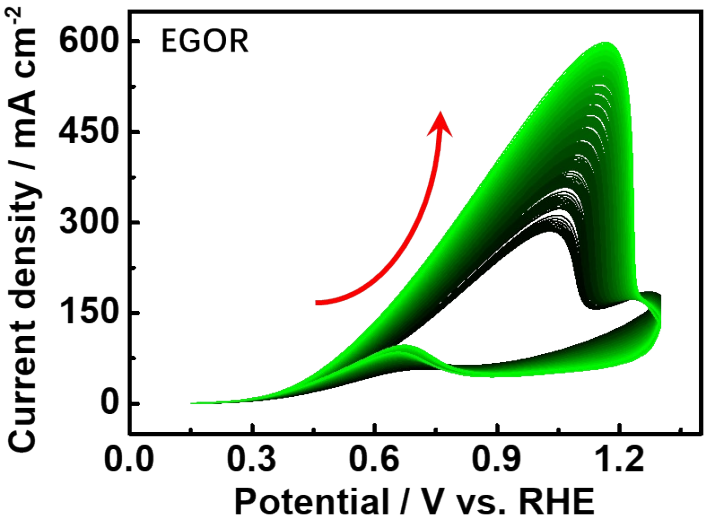

Fig. S2. Multiple cyclic voltammetry (MCV) profiles of Pt-Fe in 1 M KOH+1 M EG solution at a scan rate of 50 mV/s.

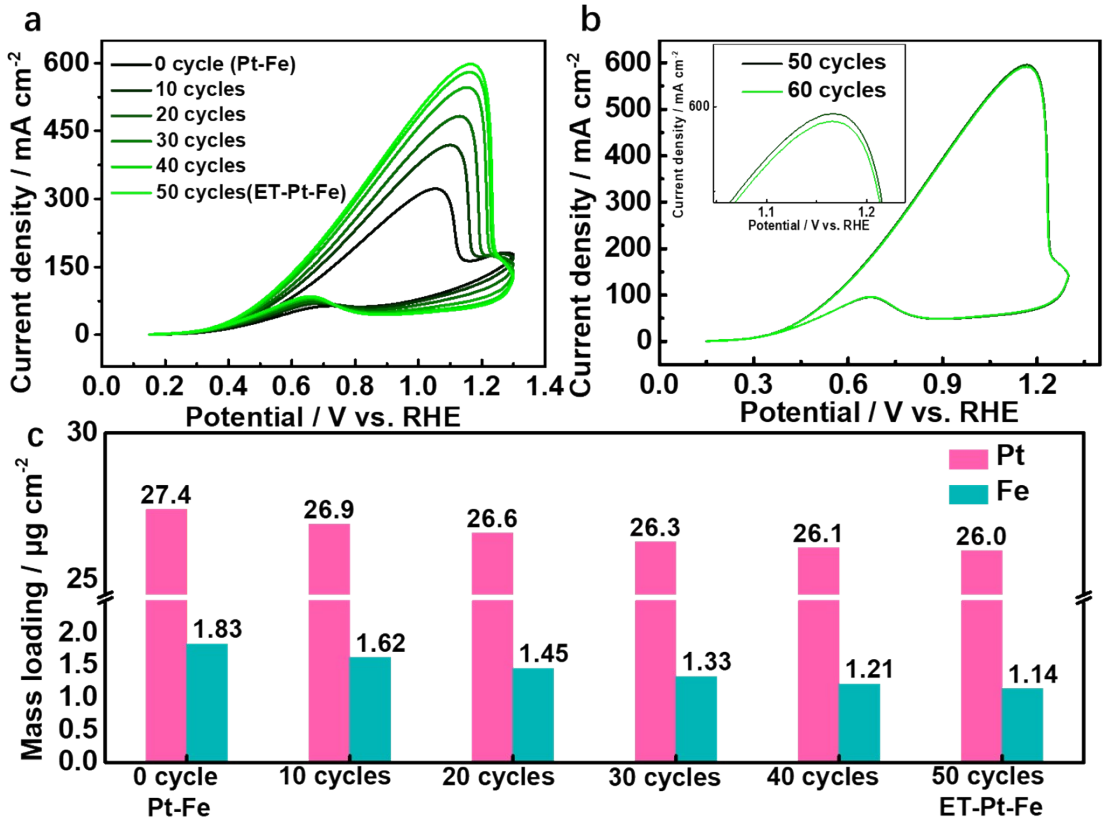

Fig. S3. (a-b) CV curves at a scan rate of 50 mV s^{-1} in N_2-saturated 1 M KOH + 1 M EG solution. (c) Plot of the change in mass loading of elements in the catalyst with the varied cycle number of electrochemical tuning.

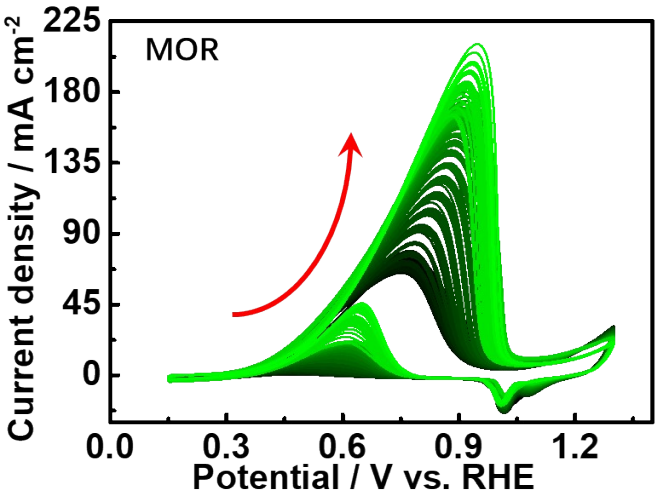

Fig. S4. MCV profiles of Pt-Fe in 1 M KOH+1 M CH_3OH solution at a scan rate of 50 mV/s.

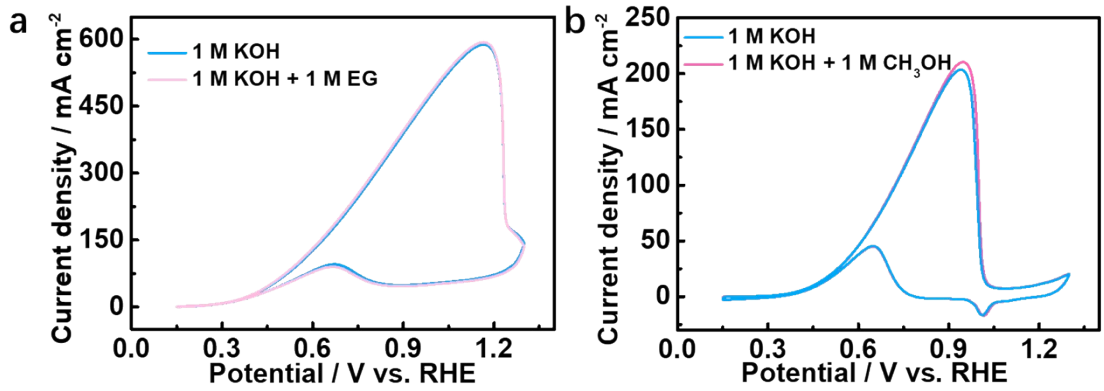

Fig. S5. (a) Comparison of EGOR performance after electrochemical tuning procedure in solution containing vs. without ethylene glycol. (b) Comparison of MOR performance after electrochemical tuning procedure in solution containing vs. without methanol.

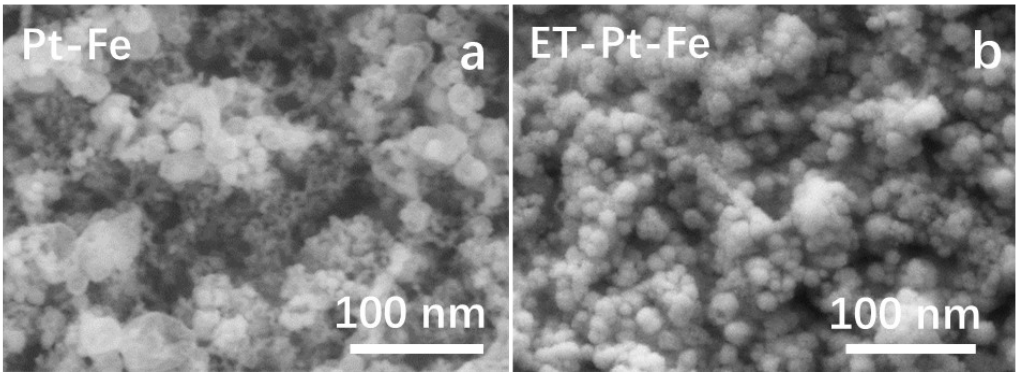

Fig. S6. Scanning electron microscope (SEM) image of (a) Pt-Fe and (b) ET-Pt-Fe.

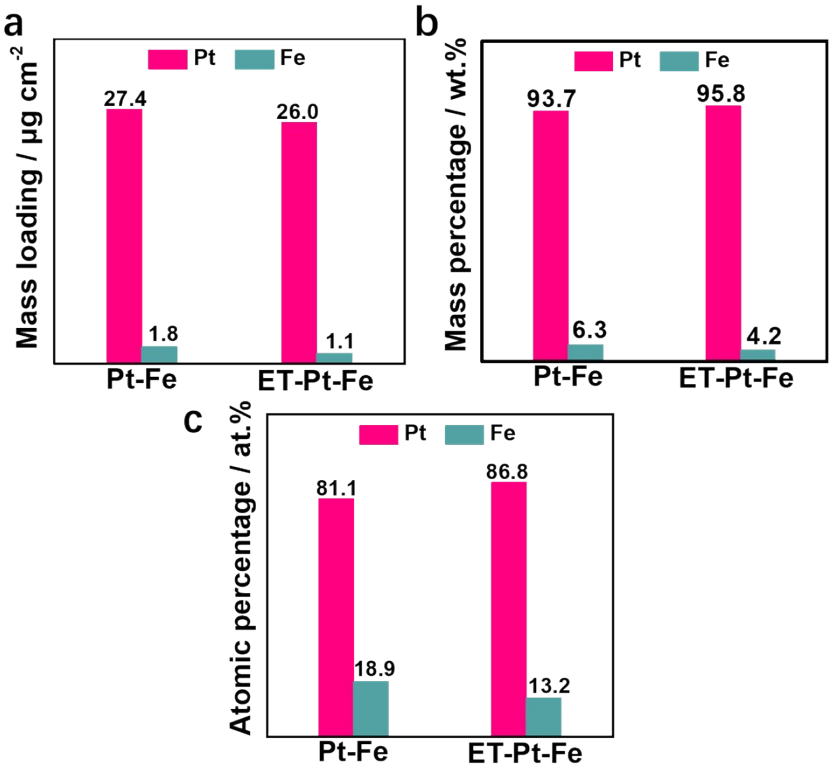

Fig. S7. (a) Mass loading of individual elements in Pt-Fe and ET-Pt-Fe from ICP-MS tests. (b) Mass percentage and (c) atomic percentage of individual elements in Pt-Fe and ET-Pt-Fe.

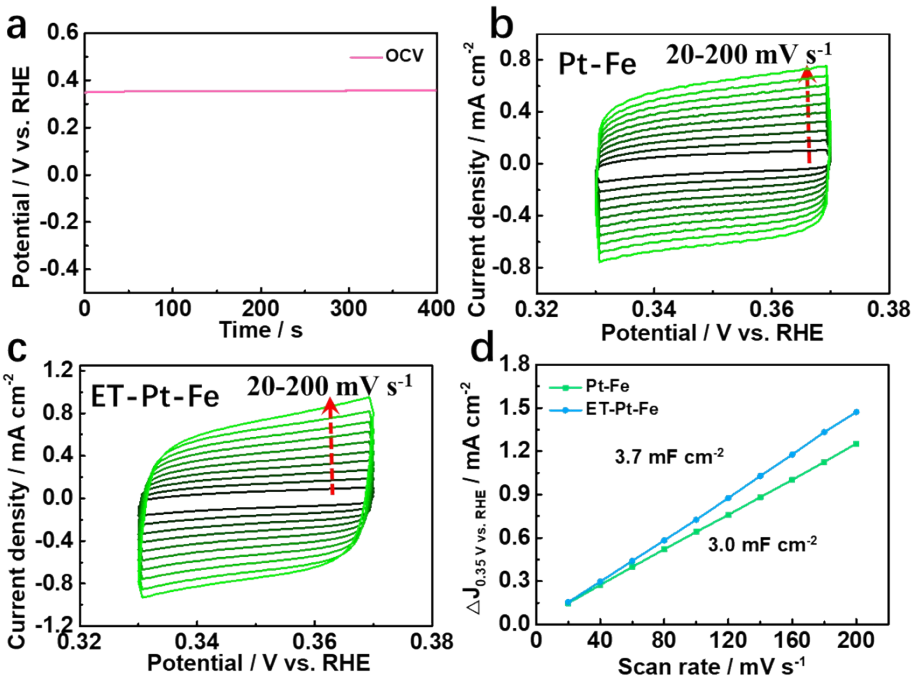

Fig. S8. (a) OCV curve of Pt-Fe. CV profiles of (b) Pt-Fe and (c) ET-Pt-Fe in 1 M KOH at various scanning rates (from 20 to 200 mV/s) within a potential range where no Faradaic process was observed. (d) The difference in current density at 0.35 V vs. RHE against the scan rate.

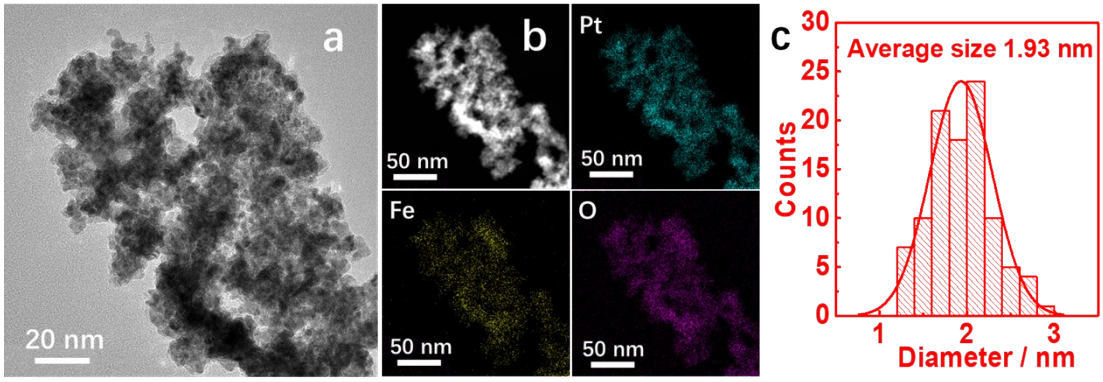

Fig. S9. (a) Transmission electron microscopy (TEM) image of ET-Pt-Fe. (b) High-angle annular dark-field scanning TEM (HAADF-STEM) and the corresponding elemental mapping images of ET-Pt-Fe. (c) Particle size distribution diagram for ET-Pt-Fe.

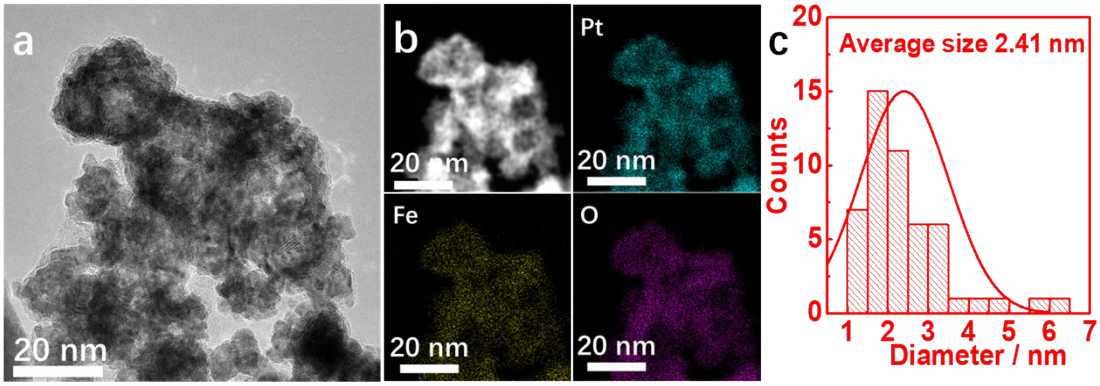

Fig. S10. (a) TEM image of Pt-Fe. (b) HAADF-STEM and the corresponding elemental mapping images of Pt-Fe. (c) Particle size distribution diagram for Pt-Fe.

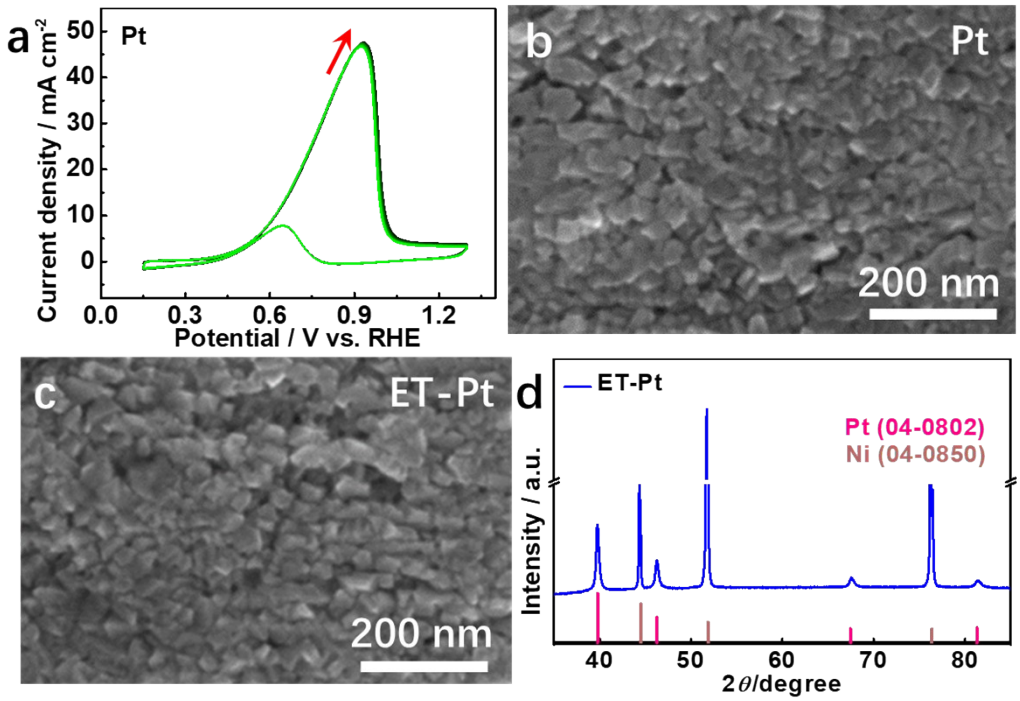

Fig. S11. (a) MCV tests of the as-prepared Pt in 1 M KOH+1 M EG solution at 50 mV/s. (b-c) SEM images of Pt and ET-Pt. (d) XRD pattern of ET-Pt.

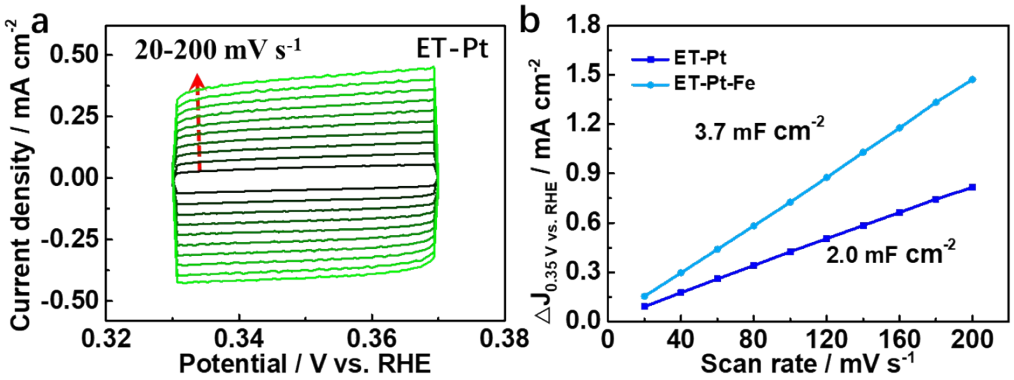

Fig. S12. (a) CV profiles of ET-Pt in 1 M KOH at various scanning rates (from 20 to 200 mV/s) within a potential range where no Faradaic process was observed. (b) The difference in current density at 0.35 V vs. RHE against the scan rate.

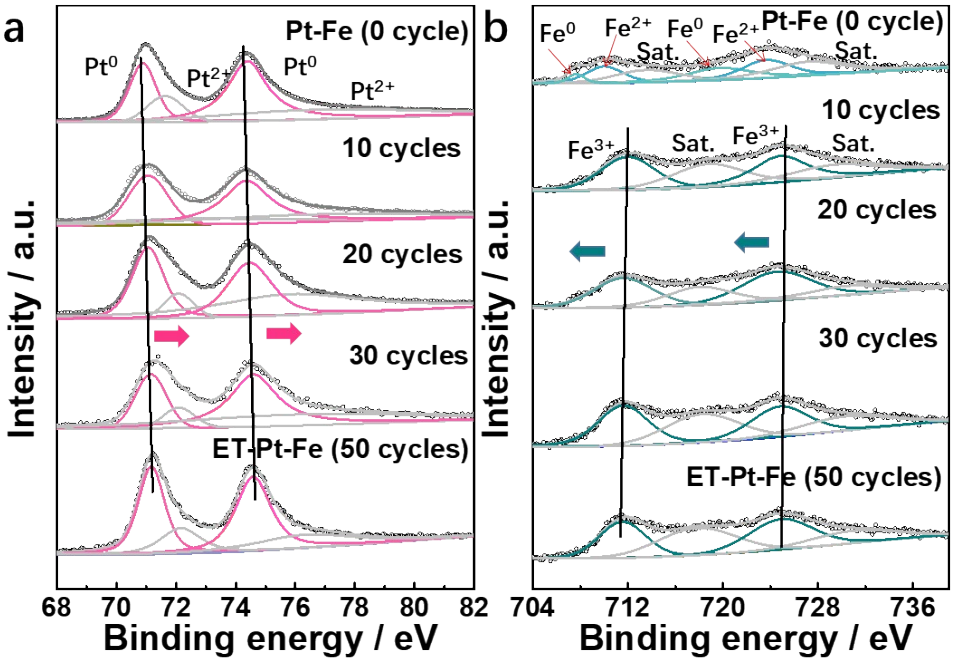

Fig. S13. XPS spectroscopy for (a) Pt 4f and (b) Fe 2p of Pt-Fe at different stages of electrochemical tuning.

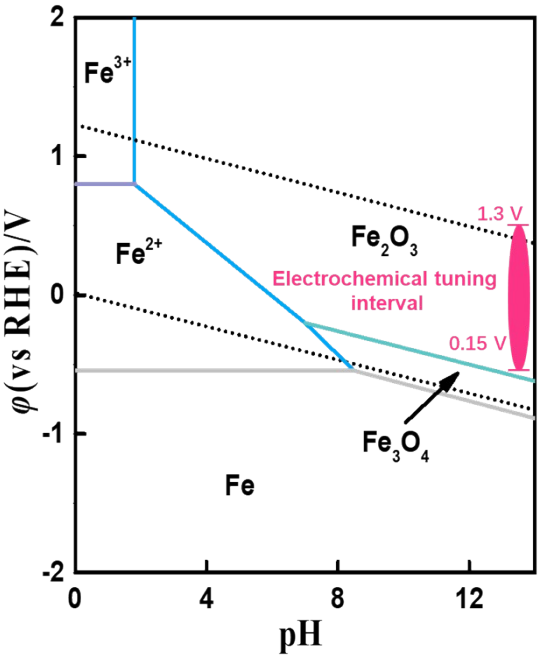

Fig. S14. Pourbaix diagram for Fe−H_2O system at 298 K.

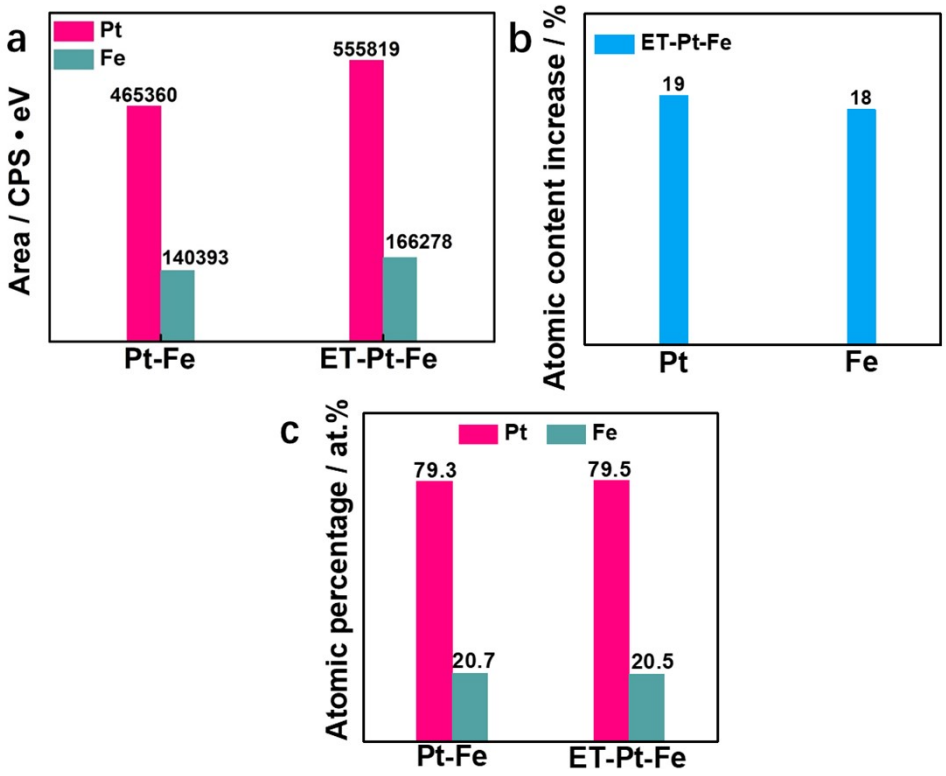

Fig. S15. (a) Integrated areas of Pt-Fe and ET-Pt-Fe in Pt 4f and Fe 2p regions. (b) Atomic content increase of individual elements on the catalyst surface after electrochemical tuning. (c) Surface atomic percentages for Pt-Fe and ET-Pt-Fe.

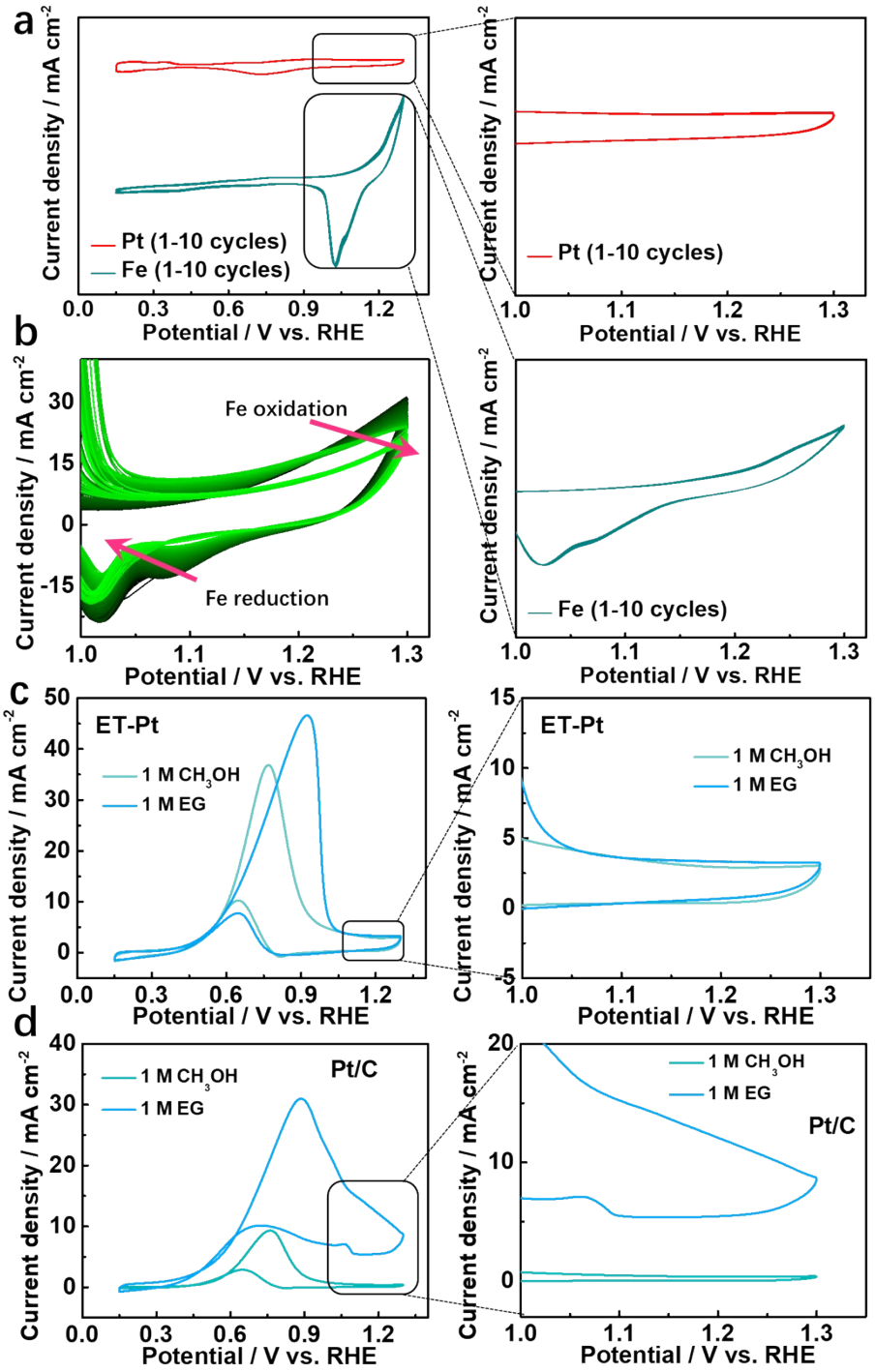

Fig. S16. (a) CV curves of pure Fe and Pt at a scan rate of 50 mV s^{-1} in N_2-saturated 1 M KOH. (b) Partial enlarged image of Pt-Fe in Fig. S4. (c) CV curves of ET-Pt and Pt/C in N_2-saturated 1 M KOH solutions containing different alcohols at a scan rate of 50 mV s^{-1}.

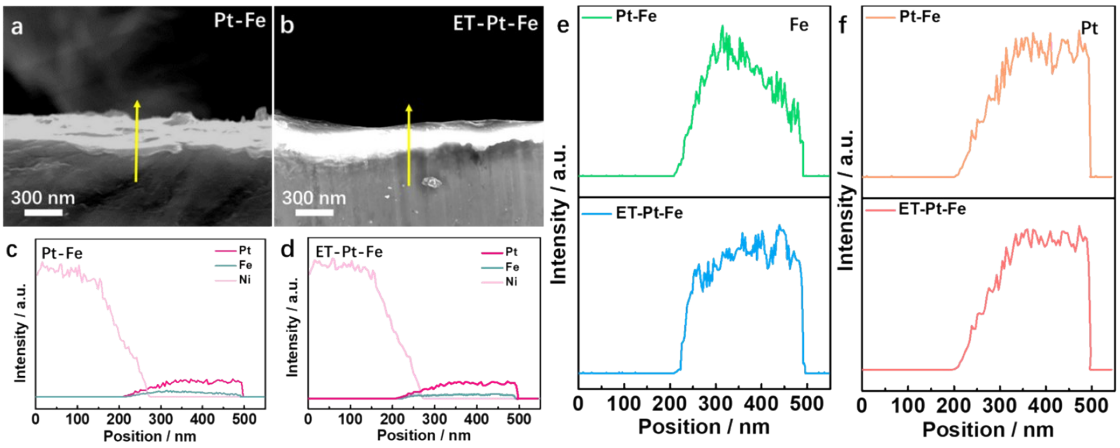

Fig. S17. Cross-sectional scanning electron microscopic image of (a) Pt-Fe and (b) ET-Pt-Fe. (c-d) Compositional profiles through the cross section along the line marked by the arrow in (a) and (b). Comparison of the distribution of (e) Fe and (f) Pt in the cross section for Pt-Fe and ET-Pt-Fe.

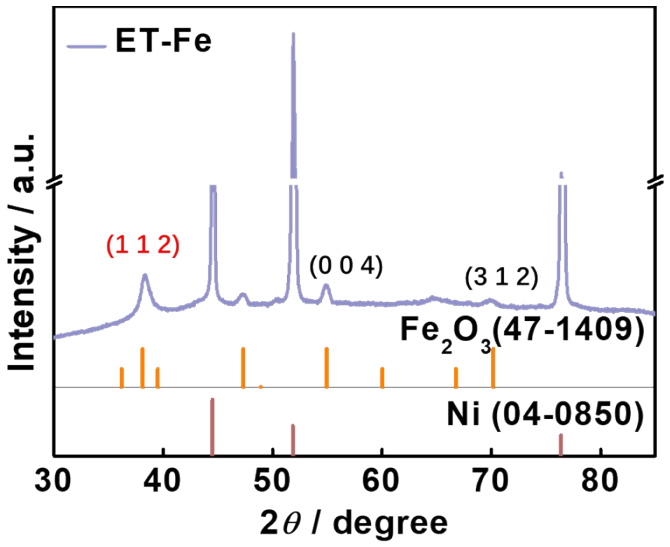

Fig. S18. The X-ray diffraction (XRD) pattern of ET-Fe.

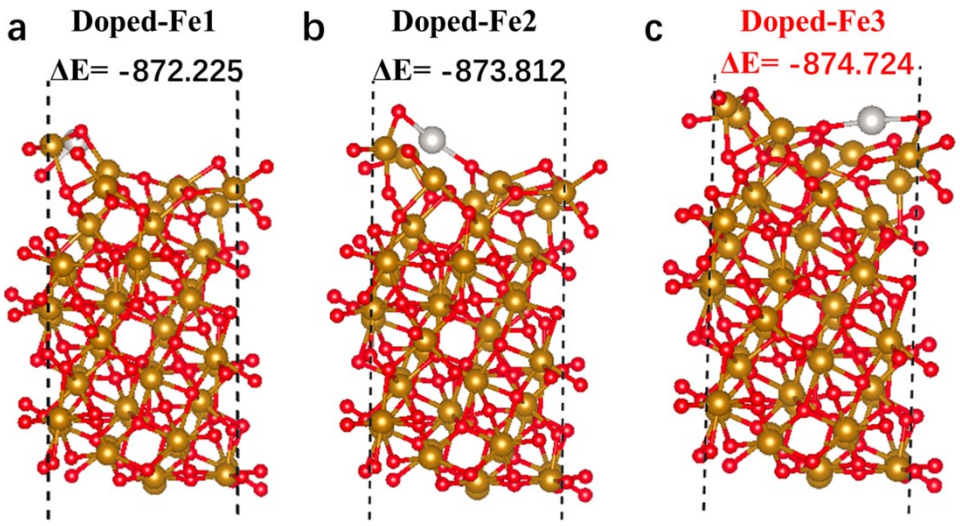

Fig. S19. The energies and optimized adsorption structures of Pt filling different Fe vacancies ((a) Fe1, (b) Fe2 and (c) Fe3) on a defective Fe_2O_3 (112) surface.

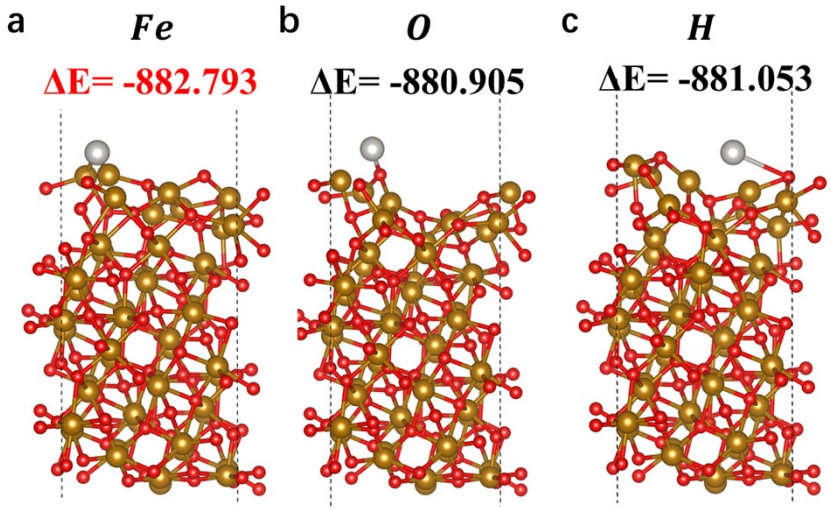

Fig. S20. Optimized adsorption structures of Pt adsorption at different sites ((a) Fe, (b) O and (c) hollow tops) on a pristine Fe_2O_3 (112) surface.

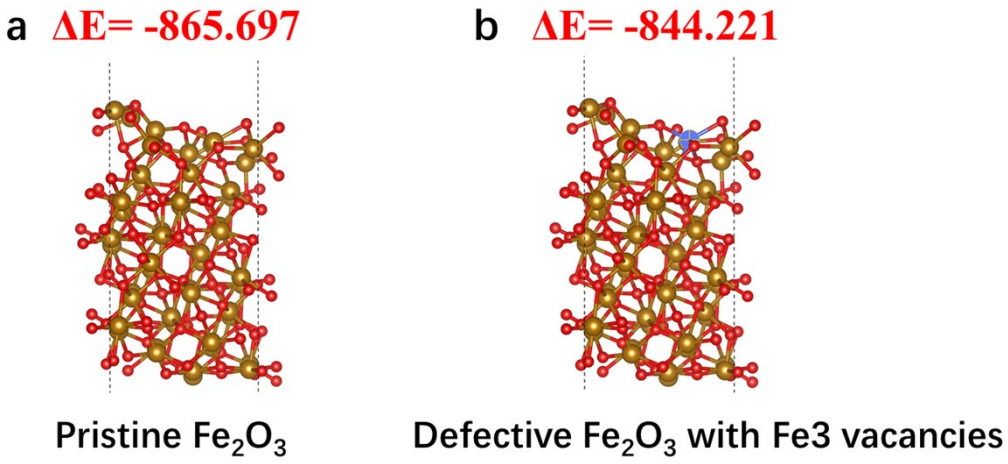

Fig. S21. Optimized adsorption structures of (a) pristine Fe_2O_3 (112) surface and (b) defective Fe_2O_3 (112) surface with Fe3 vacancies.

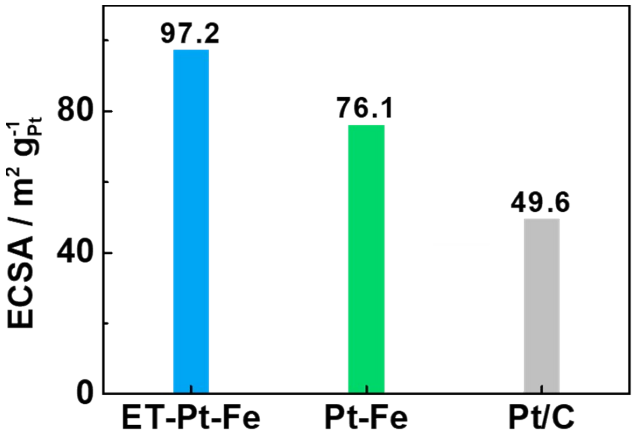

Fig. S22. Comparative plot of ECSA for different catalysts.

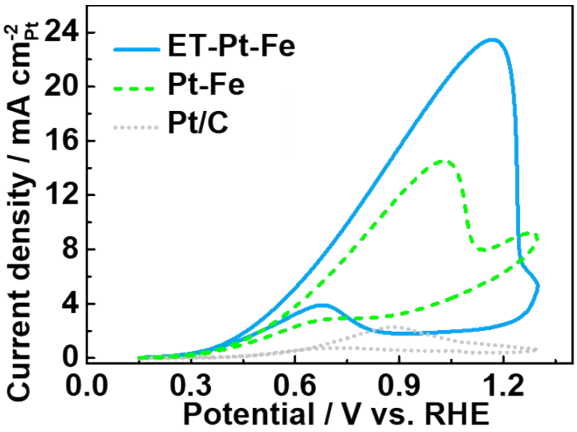

Fig. S23. Specific activity of Pt/C, Pt-Fe and ET-Pt-Fe in 1 M EG+1 M KOH solution.

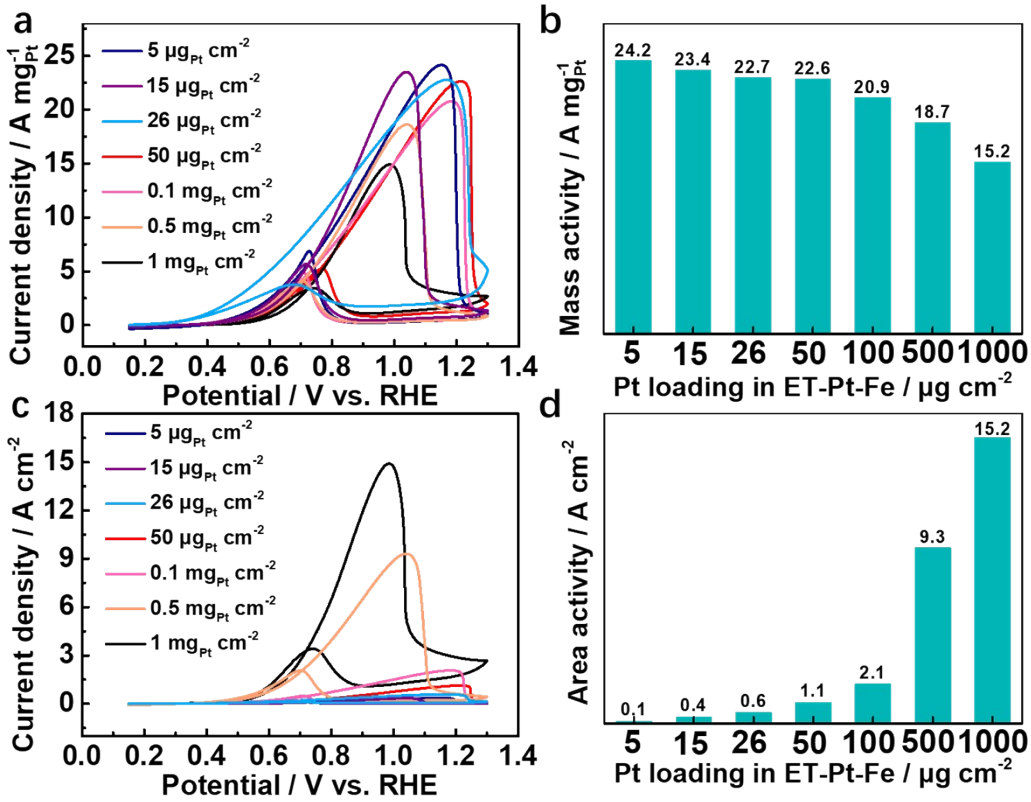

Fig. S24. (a and c) CV curves of ET-Pt-Fe with different Pt loadings at a scan rate of 50 mV s^{-1} in N_2-saturated 1 M KOH + 1 M EG solution. Plot of (b) mass activity and (d) area activity of ET-Pt-Fe with Pt loading.

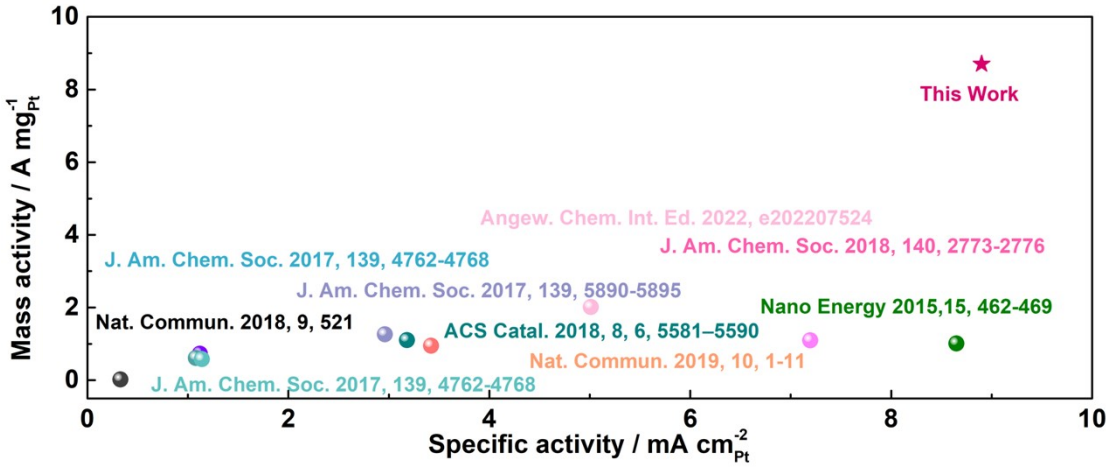

Fig. S25. Comparison chart of the performance of ET-Pt-Fe and existing methanol oxidation catalysts in the literature.

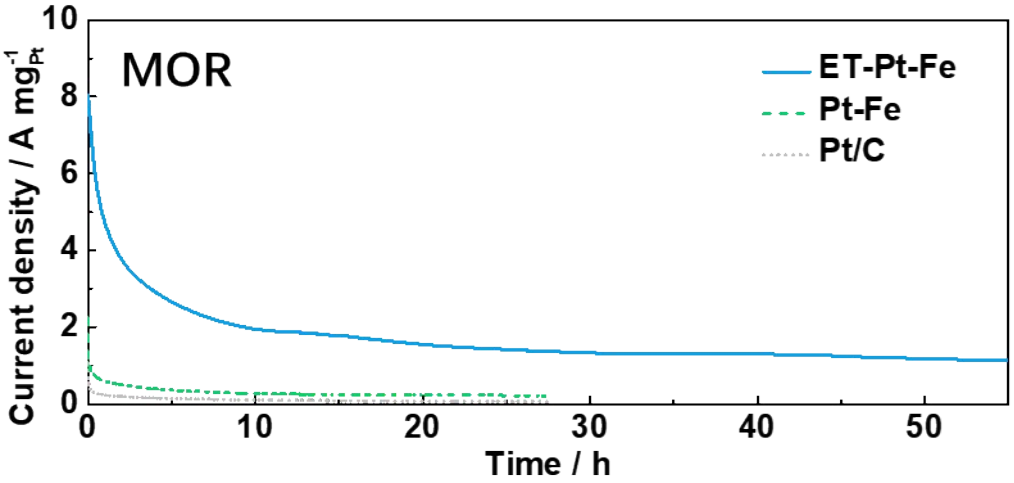

Fig. S26. Chronoamperometry curves of different catalysts for methanol oxidation in 1 M methanol+1 M KOH solution.

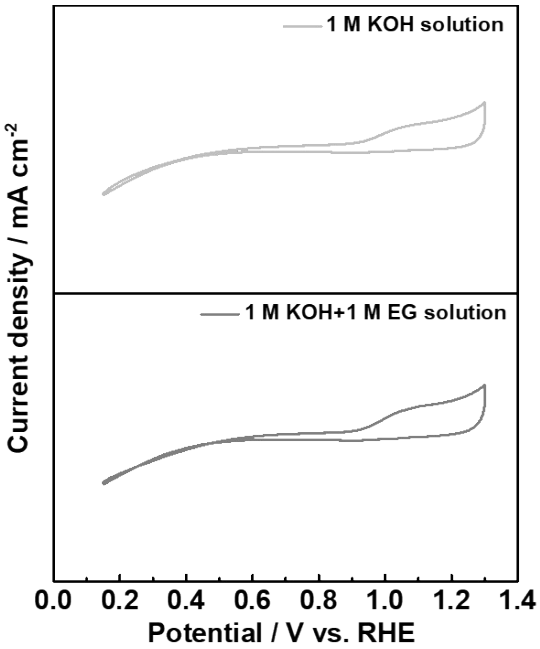

Fig. S27. CV curves of Ni foam at a scan rate of 50 mV s^{-1} in N_2-saturated 1 M KOH solution and 1 M KOH + 1 M EG solution.

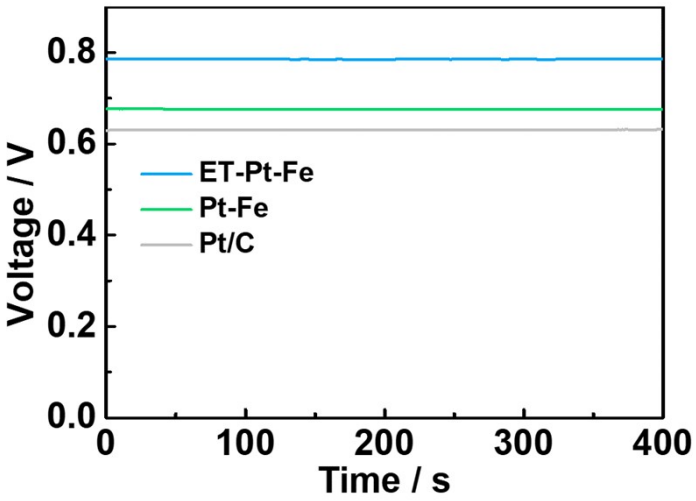

Fig. S28. Open circuit potential curves of DEGFCs.

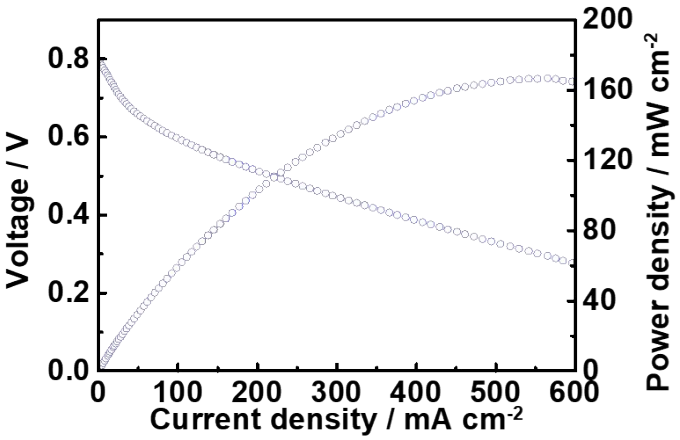

Fig. S29. Polarization and power density curves of DEGFCs using ET-Pt-Fe (0.1 mg cm^{-2}) at 1 M KOH + 1 M EG (0.5 mL min^{-1}) − O_2 (50 mL min^{-1}).

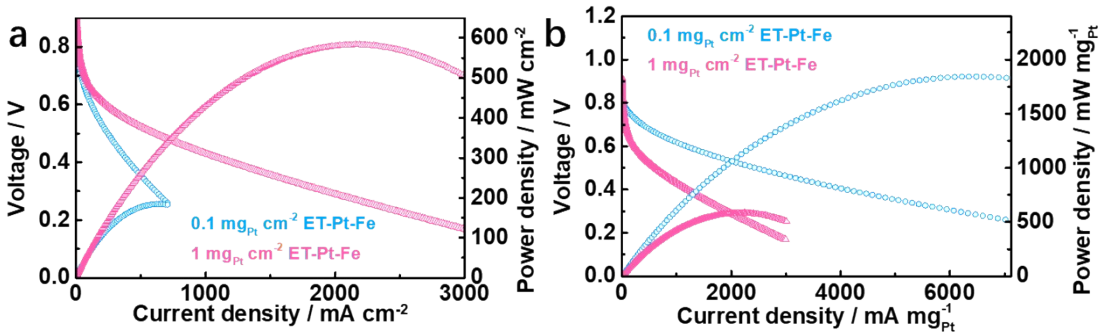

Fig. S30. Polarization and power density profiles of DEGFCs using ET-Pt-Fe (0.1 mg cm^{-2} and 1.0 mg cm^{-2}, respectively) at 6 M KOH + 3 M EG (0.5 mL min^{-1}) − O_2 (50 mL min^{-1}) based on (a) geometric area, (b) mass of Pt.

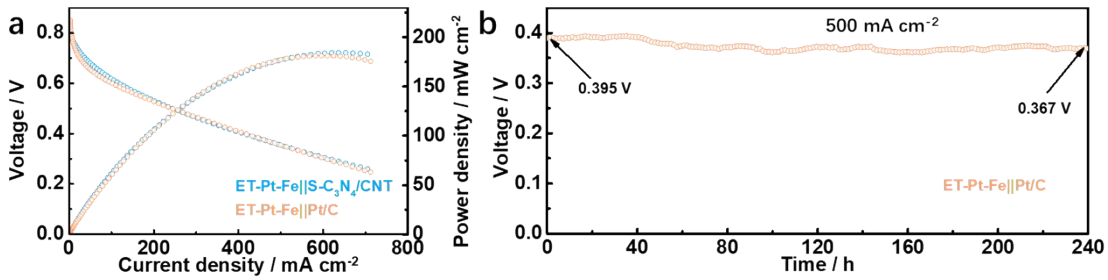

Fig. S31. (a) Polarization and power density curves of DEGFCs using ET-Pt-Fe as anode and Pt/C or S-C_3N_4/CNT as cathode at 6 M KOH + 3 M EG (0.5 mL min^{-1}) − O_2 (50 mL min^{-1}). (b) Stability test of DEGFC using ET-Pt-Fe as anode and Pt/C as cathode.

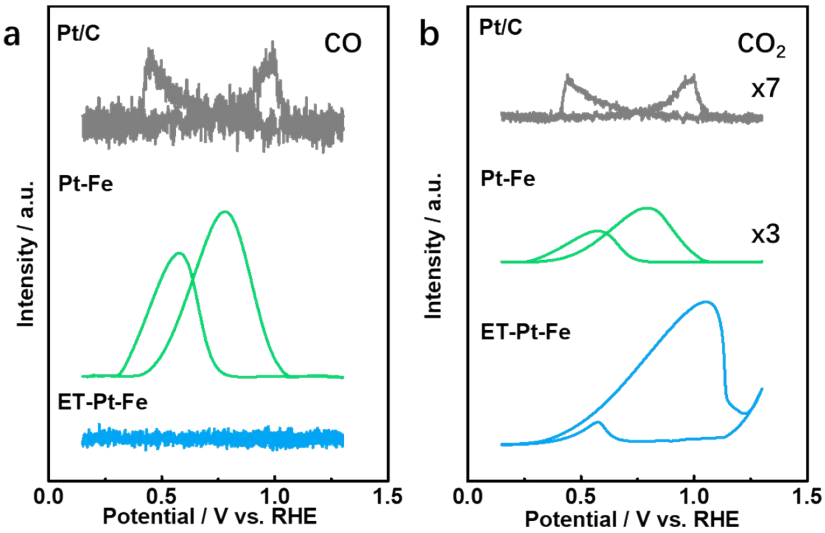

Fig. S32. Comparison of (a) CO and (b) CO_2 signal intensities during *in-situ* DEMS test of different catalysts.

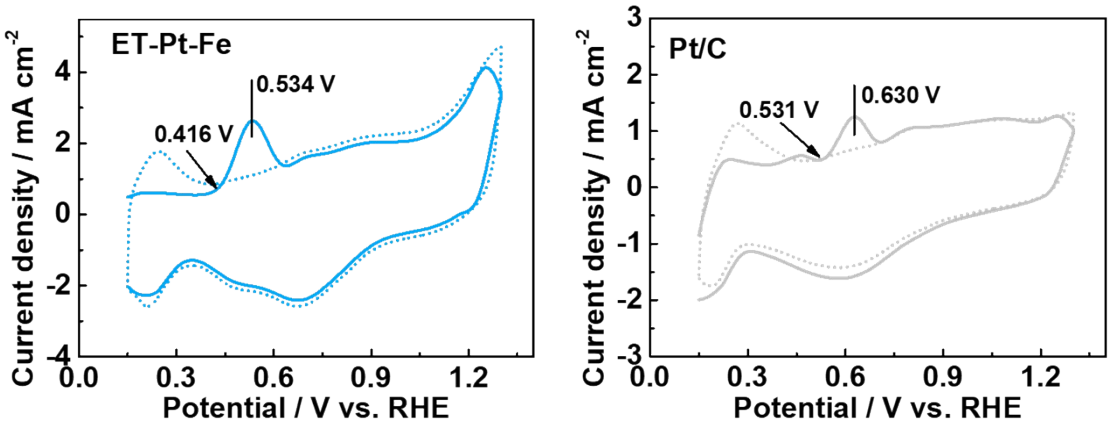

Fig. S33. Electrochemical CO stripping voltammetry of (a) ET-Pt-Fe and (b) Pt/C (The solid line represents the CV curve in CO-saturated KOH solution, and the dashed line represents the curve in nitrogen-saturated KOH solution).

Table S1. Comparison of ET-Pt-Fe with other electrocatalysts for EGOR (all results were obtained at room temperature).

Catalyst	Electrolyte	Mass activity / A mg_{Pt}^{-1} (Mass loading)	Specific activity / mA cm_{Pt}^{-2}	Ref.
ET-Pt-Fe	1 M KOH + 1 M EG	**22.7 (26 μg_{Pt} cm^{-2})** **15.2 (1000 μg_{Pt} cm^{-2})**	**23.4** **15.6**	**This work**
RhCu nanoboxes	1 M KOH + 1 M EG	0.77 (53.7 μg_{Rh} cm^{-2})	1.54	7
$Pt_{81}Rh_{19}$ NDs	0.5 M KOH + 0.5 M EG	1.5 (85 μg_{Pt} cm^{-2})	-	8
PtRuPd NSs	0.5 M KOH + 0.5 M EG	1.368 (84.9 μg_{total} cm^{-2})	-	9
AuPt core-shell structures	1 M KOH + 0.75 M EG	0.973	2.51	10
$Pt_{31}Cu_{69}$ NWs	0.5 M KOH + 0.5 M EG	1.46 (15.8 μg_{Pt} cm^{-2})	-	11
Au-Pd@Pd NCs	0.5 M KOH + 0.5 M EG	0.535 (171.4 μg_{total} cm^{-2})	-	12
PdRuCu NAs	0.5 M KOH + 0.5 M EG	1.16	2.51	13
Ultrathin $Pt_{32}Pd_{48}Ni_{20}$ NSs	0.5 M KOH + 0.5 M EG	9.77 (81.6 μg_{Pd+Pt} cm^{-2})	-	14
$Pd_{62}Au_{21}Ni_{17}$	0.5 M KOH + 0.5 M EG	6.63 (11.8 μg_{Pd+Au} cm^{-2})	-	15

PdPt nanowire	0.5 M KOH + 0.5 M EG	3.37 (25.5 μg_{Pt+Pd} cm^{-2})	-	16
Pt_4Rh-L NCs	1 M KOH + 1 M EG	5.13 (28.6 μg_{Pt} cm^{-2})	11.6	17
Pd-PdSe HNSs	1 M KOH + 1 M EG	8.6	15.7	18
Pt_3Mn	0.5 M KOH + 0.5 M EG	0.24 (4.56 μg_{Pt} cm^{-2})	1.32	19
PdCu-2 NSs	1 M KOH + 1 M EG	5.8 (14.3 μg_{Pd} cm^{-2})	14.3	20
$PtRh_{0.02}$@Rh	0.1 M KOH + 0.5 M EG	1.25 (110 μg_{Pt+Rh} cm^{-2})	5.8	21
Pd_2Ag_1	1 M KOH + 1 M EG	4.2	14.8	22
$Pt_{52}Cu_{48}$ HTNCs	1 M KOH + 1 M EG	5.7	11.2	23
Pt_3Cu NCs	1 M KOH + 1 M EG	5.2 (4 μg_{Pt} cm^{-2})	9.7	24
Pd_9Ru_1 NSs	1 M KOH + 1 M EG	5.9 (10 μg_{Pd} cm^{-2})	9.4	25
PdAg NFs	1 M KOH + 1 M EG	3.6 (10 μg_{Pd} cm^{-2})	1.5	26
Pd-Ru nanocages	1 M KOH + 1 M EG	5.5	-	27
$Pd_{58}Cu_{32}Ir_{10}$ NCs	1 M KOH + 1 M EG	4.5 (31 μg_{Pd} cm^{-2})	-	28
PtPbBi-HPN-1	1 M NaOH + 1 M EG	12.22 (20 μg_{Pt} cm^{-2})	-	29
Pt-Co EDNC/C	0.5 M KOH + 0.5 M EG	2.5 (10 μg_{Pt} cm^{-2})	7.82	30

Pt_3Cu NCs	1 M KOH + 1 M EG	5.2 (4 μg_{Pt} cm^{-2})	9.7	[24]
Us PtCu@C	0.5 M KOH + 1 M EG	8.5 (4.3 μg_{Pt} cm^{-2})	3.7	[31]
$PtNi_{0.67}Pd_{0.26}$ NWs/C	0.1 M $HClO_4$ + 0.2 M EG	0.65 (10.2 μg_{Pt+Pd} cm^{-2})	0.42	[32]
0.4%Mo/Pt_3Mn	0.1 M HClO4 + 0.5 M EG	0.23 (10 μg_{Pt} cm^{-2})	1.23	[33]
Pd_3Pb_1@Pd aerogel	1 M KOH + 0.5 M EG	6.4	-	[34]
Pd_2Pb NCs	1 M KOH + 1 M EG	4.06	16.8	[35]

Table S2. Direct glycol fuel cell and direct methanol fuel cell performance reported in the literature.

Catalyst	Noble metal loading / mg cm^{-2}	Membrane (active area)	Operating temperature / °C	Flow rate / mL min^{-1}	Anolyte	Peak power density / mW cm^{-2}	Ref.
ET-Pt-Fe	**0.1**	**Fumasep FAAM-15 (1 cm^2)**	**80**	**EG: 0.5; O_2: 50**	**6 M KOH+3 M EG** **1 M KOH+1 M EG**	**185.8** **165.2**	**This work**
PtBiNiCoSn/C	1	Polybenzimidazole (1 cm^2)	80	-	6 M KOH+2 M EG	8.49	[36]
PdAg/C	1.2	Nafion 117	-	EG: 0.05; O_2: 0.1	1 M KOH+1 M EG	5.2	[37]
Pd nanocubes/C	1.2	Nafion 117	-	EG: 0.05; O_2: 0.1	1 M KOH+1 M EG	5.2	[37]
PtCo(1:13)/rGO	2	Nafion 117 (5 cm^2)	100	EG: 1; O_2: 200	1 M H_2SO_4+2 M EG	8.4	[38]
PtSn/C (90:10)	1	Nafion 117	100	EG: 1	10 wt.% KOH+2 M EG	8.4	[39]
PtRu/C (50:50)	1	Nafion® 117 (5 cm^2)	70	-	1 M KOH+1 M EG	5.8	[40]
PtPdAuNiCo/C	0.7	KOH-doped PBI film (1 cm^2)	80	EG: 2; O_2: 200	6 M KOH +2 M EG	8.38	[41]
$Pd_{52}Ni_{48}$/NSCNT	2	Polymethylmethacrylate (0.24 cm^2)	-	EG: 0.05; O_2: 0.2	1 M KOH+0.5 M EG	62.8	[42]

Au/C	1	Tokuyama A201 (5 cm^2)	50	EG: 4; O_2: 400	2 M KOH+1 M EG	7.3	[43]
Au/C	1	Tokuyama A201 (5 cm^2)	50		2 M KOH+0.1 M EG	1.3	[43]
Pd_2Ni_3/C	1	Polybenzimidazole (1 cm^2)	60	EG: 1; O_2: 100	1 M KOH+1 M EG	44	[44]
Cu@Pd	1.5	-	-	-	0.3 M KOH+1 M EG	19.1	[45]
PtSn/WO_3-MWCNT	0.332	Nafion 117	60	EG: 2.5; O_2: 200	0.5 M H_2SO_4+1 M EG	20.5	[46]
Pd nanocubes/C	1.2	Nafion 117	-	EG: 0.05; O_2: 0.1	1 M KOH+1 M EG	14.4	[37]
PdAg/C	0.46	Nafion 117	-	EG: 0.05; O_2: 0.1	1 M KOH+1 M EG	9.66	[37]
PdNi/C	0.4	Nafion 117 (1 cm^2)	60	EG: 2; O_2: 100	7 M KOH+3 M EG	22	[47]
Pt/C	0.8	ADP-Morgane® (5 cm^2)	20	EG: 2; O_2: 20	4 M KOH+2 M EG	4	[48]
Pt/C	1	Nafion 117 (9 cm^2)	60	methanol: 20; O_2: 200	1 M CH_3OH	26	[49]
PtMo-CeO_x-NA	0.8	Nafion 115 (6.25 cm^2)	70	methanol: 1; O_2: 500	1 M CH_3OH	15	[50]
Pt/C	2	Nafion 117 (10 cm^2)	80	methanol: 1; O_2: 300	1 M CH_3OH	47	[51]
Au@Ag-S@Pt	2	Nafion 117	80	methanol: 1;	1 M CH_3OH	65	[51]

		(10 cm^2)		O_2: 300			
Pt/graphene-TiO_2	2.5	-	-	-	2 M CH_3OH	12	[52]
Pt-Ni_2P/C	1	Nafion 117 (9 cm^2)	60	methanol: 20; O_2: 200	1 M CH_3OH	65	[49]
Pt-CoP/C	1.2	Nafion 117 (9 cm^2)	80	methanol: 2; O_2: 200	2 M CH_3OH	88.5	[53]
Pt/$Ti_{0.9}Sn_{0.1}O_2$-C	1	Nafion 117 (5 cm^2)	80	methanol: 3; O_2: 600	2 M CH_3OH	97	[54]
ASP Pt NWs	2	Nafion 117 (5 cm^2)	80	methanol: 1; O_2: 100	1 M CH_3OH	63.9	[55]
Pt@RFC	0.75	Nafion 117 (25 cm^2)	80	methanol: 13.5; O_2: 1000	1 M CH_3OH	87.2	[56]
Pt-$NiTiO_3$/C	0.5	Nafion 117 (36 cm^2)	80	methanol: 3; O_2: 100	1 M CH_3OH	32.8	[57]
PtRu/C-20% IrO_2	0.5	Nafion 117 (5 cm^2)	60	methanol: 2; O_2: 100	2 M CH_3OH	22	[58]
PtRuMo/CNTs	2	Nafion 115 (5 cm^2)	80	methanol: 3; O_2: 150	2 M CH_3OH	61.3	[59]
PtCu NWs	0.6	Nafion 115 (1 cm^2)	80	methanol: 1; O_2: 100	1 M CH_3OH	49.7	[60]
Pd-$Sn_{0.5}$	0.5	- (5 cm^2)	-	-	1 M CH_3OH	10.2	[61]
Pt_8Ti-TiO_2/C	0.1	Nafion 117 (5 cm^2)	80	methanol: 300; O_2: 300	2 M CH_3OH	48.7	[62]
Pt-Sn-Ce/C	2.2	Nafion 115 (5 cm^2)	80	methanol: 2.5; O_2: 200	1 M CH_3OH	83	[63]

References

1. H. Lei, M. Cui and Y. Huang, *ACS Appl. Mater. Interfaces*, 2022, **14**, 34793-34801.
2. G. Kresse and J. Furthmüller, *Phys. Rev. B*, 1996, **54**, 11169-11186.
3. G. Kresse and D. Joubert, *Phys. Rev. B*, 1999, **59**, 1758-1775.
4. J. P. Perdew, K. Burke and M. Ernzerhof, *Phys. Rev. Lett.*, 1996, **77**, 3865-3868.
5. H. J. Monkhorst and J. D. Pack, *Phys. Rev. B*, 1976, **13**, 5188-5192.
6. J. Moellmann and S. Grimme, *J. Phys. Chem. C*, 2014, **118**, 7615-7621.
7. B. Qiao, T. Yang, S. Shi, N. Jia, Y. Chen, X. Chen, Z. An and P. Chen, *Small*, 2021, **17**, e2006534.
8. Y.-X. Xie, S.-Y. Cen, Y.-T. Ma, H.-Y. Chen, A.-J. Wang and J.-J. Feng, *J. Colloid Interf. Sci.*, 2020, **579**, 250-257.
9. J. J. Duan, X. X. Zheng, H. J. Niu, J. J. Feng, Q. L. Zhang, H. Huang and A. J. Wang, *J. Colloid Interf. Sci.*, 2020, **560**, 467-474.
10. S. Dutta, C. Ray, S. Sarkar, A. Roy, R. Sahoo and T. Pal, *Electrochim. Acta*, 2015, **180**, 1075-1084.
11. W. Zhang, Q. Dong, H. Lu, B. Hu, Y. Xie and G. Yu, *J. Alloy Compd.*, 2017, **727**, 475-483.
12. Q. Liu, Y.-R. Xu, A.-J. Wang and J.-J. Feng, *Int. J. Hydrogen Energy*, 2016, **41**, 2547-2553.
13. R.-L. Zhang, J.-J. Duan, Z. Han, J.-J. Feng, H. Huang, Q.-L. Zhang and A.-J. Wang, *Appl. Surf. Sci.*, 2020, **506**, 144791.
14. J. Lai, F. Lin, Y. Tang, P. Zhou, Y. Chao, Y. Zhang and S. Guo, *Adv. Energy Mater.*, 2019, **9**, 1800684.
15. S. Li, J. Lai, R. Luque and G. Xu, *Energy Environ. Sci.*, 2016, **9**, 3097-3102.
16. W. Hong, C. Shang, J. Wang and E. Wang, *Energy Environ. Sci.*, 2015, **8**, 2910-2915.
17. F. Gao, Y. Zhang, P. Song, J. Wang, T. Song, C. Wang, L. Song, Y. Shiraishi and Y. Du, *J. Mater. Chem. A*, 2019, **7**, 7891-7896.
18. Y. Qin, W. Zhang, F. Wang, J. Li, J. Ye, X. Sheng, C. Li, X. Liang, P. Liu, X. Wang, X. Zheng, Y. Ren, C. Xu and Z. Zhang, *Angew. Chem. Int. Ed.*, 2022, **61**, e202200899.
19. Y. Wang, M. Zheng, H. Sun, X. Zhang, C. Luan, Y. Li, L. Zhao, H. Zhao, X. Dai,

J.-Y. Ye, H. Wang and S.-G. Sun, *Appl. Catal. B-Environ.*, 2019, **253**, 11-20.

20. K. Zhang, C. Wang, H. You, B. Zou, S. Guo, S. Li and Y. Du, *Chem. Eng. J.*, 2022, **438**, 135666.

21. X. Jiang, Z. M. Dong, Q. Zhang, G. R. Xu, J. P. Lai, Z. J. Li and L. Wang, *J. Mater. Chem. A*, 2022, **10**, 20571-20579.

22. F. Gao, Y. Zhang, P. Song, J. Wang, C. Wang, J. Guo and Y. Du, *J. Power Sources*, 2019, **418**, 186-192.

23. H. Xu, P. Song, F. Gao, Y. Shiraishi and Y. Du, *Nanoscale*, 2018, **10**, 8246-8252.

24. H. Xu, C. Liu, P. Song, J. Wang, F. Gao, Y. Zhang, Y. Shiraishi, J. Di and Y. Du, *Chem. Asian J.*, 2018, **13**, 626-630.

25. B. Zou, F. Gao, H. You, Z. Li, Y. Zhang, Z. Wu, T. Song and Y. Du, *J. Colloid Interf. Sci.*, 2021, **601**, 42-49.

26. C. Zhai, J. Hu and M. Zhu, *Electroanal. Chem.*, 2017, **806**, 1-7.

27. M. Zhao, Z. Lyu, M. Xie, Z. D. Hood, Z. Cao, M. Chi and Y. Xia, *Small Methods*, 2020, **4**, 1900843.

28. C. Chen, T. Song, H. Shang, Q. Liu, M. Yuan, C. Wang and Y. Du, *Int. J. Hydrogen Energy*, 2020, **45**, 26920-26928.

29. Z. Zhu, F. Liu, J. Fan, Q. Li, Y. Min and Q. Xu, *ACS Appl. Mater. Interfaces*, 2020, **12**, 52731-52740.

30. H. Du, K. Wang, P. Tsiakaras and P. K. Shen, *Appl. Catal. B- Environ.*, 2019, **258**, 117951.

31. J. Gao, M. Mao, P. Li, R. Liu, H. Song, K. Sun and S. Zhang, *ACS Appl. Mater. Interfaces*, 2020, **12**, 6298-6308.

32. N. Zhang, Y. Zhu, Q. Shao, X. Zhu and X. Huang, *J. Mater. Chem. A*, 2017, **5**, 18977-18983.

33. Y. Wang, H. Zhuo, H. Sun, X. Zhang, X. Dai, C. Luan, C. Qin, H. Zhao, J. Li, M. Wang, J.-Y. Ye and S.-G. Sun, *ACS Catal.*, 2018, **9**, 442-455.

34. C. Zhu, Q. Shi, S. Fu, J. Song, D. Du, D. Su, M. H. Engelhard and Y. Lin, *J. Mater. Chem. A*, 2018, **6**, 7517-7521.

35. H. Xu, P. Song, C. Fernandez, J. Wang, M. Zhu, Y. Shiraishi and Y. Du, *ACS Appl. Mater. Interfaces*, 2018, **10**, 12659-12665.

36. L. Miao, Y. Cheng, Y. Liu, X. Li, L. Zhang and W. Wang, *J. Alloy Compd.*, 2024, DOI: 10.1016/j.jallcom.2024.173951.

37. A. López–Coronel, E. Ortiz–Ortega, L. J. Torres–Pacheco, M. Guerra–Balcázar, L. G. Arriaga, L. Álvarez–Contreras and N. Arjona, *Electrochim. Acta*, 2019, **320**, 134622.

38. R. Baronia, J. Goel, Baijnath, V. Kataria, S. Basu and S. K. Singhal, *Int. J. Hydrogen Energy*, 2019, **44**, 10023-10032.

39. L. L. de Souza, A. O. Neto and C. A. L. G. de O. Forbicini, *Int. J. Electrochem. Sc.*, 2017, **12**, 11855-11874.

40. J. C. M. Silva, S. Ntais, V. Rajaraman, É. Teixeira-Neto, Â. A. Teixeira-Neto, A. O. Neto, R. M. Antoniassi, E. V. Spinacé and E. A. Baranova, *Electrocatalysis*, 2019, **10**, 203-213.

41. Y. Cheng, Y. Sun, X. Deng, M. Zhang, L. Zhang and W. Wang, *Int. J. Hydrogen Energy*, 2023, **48**, 8156-8164.

42. T. Raj kumar, G. Gnana kumar and A. Manthiram, *Adv. Energy Mater.*, 2019, **9**, 1803238.

43. L. Xin, Z. Zhang, J. Qi, D. Chadderdon and W. Li, *Appl. Catal. B-Environ.*, 2012, **125**, 85-94.

44. S. Y. Shen, T. S. Zhao, J. B. Xu and Y. S. Li, *J. Power Sources*, 2010, **195**, 1001-1006.

45. J. Maya-Cornejo, E. Ortiz-Ortega, L. Álvarez-Contreras, N. Arjona, M. Guerra-Balcázar, J. Ledesma-García and L. G. Arriaga, *Chem. Commun.*, 2015, **51**, 2536-2539.

46. K. Miecznikowski, *Arab. J. Chem.*, 2020, **13**, 1020-1031.

47. L. An, T. S. Zhao, S. Y. Shen, Q. X. Wu and R. Chen, *Int. J. Hydrogen Energy*, 2010, **35**, 4329-4335.

48. L. Demarconnay, S. Brimaud, C. Coutanceau and J. M. Léger, *Electroanal. Chem.*, 2007, **601**, 169-180.

49. J. Chang, L. Feng, C. Liu, W. Xing and X. Hu, *Energy Environ. Sci.*, 2014, **7**, 1628–1632.

50. P. Wang, H. Cui and C. Wang, *Chem. Eng. J.*, 2022, **429**, 132435.

51. Y. Feng, H. Liu and J. Yang, *Sci. Adv.*, 2017, **3**, e1700580.

52. L. Zhao, Z.-B. Wang, J. Liu, J.-J. Zhang, X.-L. Sui, L.-M. Zhang and D.-M. Gu, *J. Power Sources*, 2015, **279**, 210-217.

53. J. Chang, L. Feng, K. Jiang, H. Xue, W.-B. Cai, C. Liu and W. Xing, *J. Mater. Chem. A*, 2016, **4**, 18607-18613.

54. Y. Li, C. Liu, Y. Liu, B. Feng, L. Li, H. Pan, W. Kellogg, D. Higgins and G. Wu, *J. Power Sources*, 2015, **286**, 354-361.

55. K. Lin, Y. Lu, S. Du, X. Li and H. Dong, *Int. J. Hydrogen Energy*, 2016, **41**, 7622-7630.

56. K. Li, Z. Jin, J. Ge, C. Liu and W. Xing, *J. Mater. Chem. A*, 2017, **5**, 19857-19865.

57. T. Kumaresan, T. Velumani, M. Chandran, K. Palaniswamy, A. Thirkell, A. Fly, R. Chen and S. Sundaram, *Mater. Lett.*, 2020, **276**, 128222.

58. V. Baglio, D. Sebastián, C. D'Urso, A. Stassi, R. S. Amin, K. M. El-Khatib and A. S. Aricò, *Electrochim. Acta*, 2014, **128**, 304-310.

59. S. Chen, F. Ye and W. Lin, *Int. J. Hydrogen Energy*, 2010, **35**, 8225-8233.

60. K. Wang, D. Huang, Y. Guan, F. Liu, J. He and Y. Ding, *ACS Catal.*, 2021, **11**, 14428-14438.

61. S. Chen, N. Liu, J. Zhong, R. Yang, B. Yan, L. Gan, P. Yu, X. Gui, H. Yang, D. Yu, Z. Zeng and G. Yang, *Angew. Chem. Int. Ed.*, 2022, **61**, e202209693.

62. J. Sanetuntikul, K. Ketpang and S. Shanmugam, *ACS Catal.*, 2015, **5**, 7321-7327.

63. A. Murthy, E. Lee and A. Manthiram, *Appl. Catal. B-Environ.*, 2012, **121-122**, 154-161.